# Flexural and tensile properties of a glass fiber-reinforced ultra-high-strength concrete: an experimental, micromechanical and numerical study

M. Jason Roth\*, Thomas R. Slawson and Omar G. Flores

*U.S. Army Engineer Research and Development Center, Vicksburg, MS 39180, USA*

**Abstract.** The focus of this research effort was characterization of the flexural and tensile properties of a specific ultra-high-strength, fiber-reinforced concrete material. The material exhibited a mean unconfined compressive strength of approximately 140 MPa and was reinforced with short, randomly distributed alkali resistant glass fibers. As a part of the study, coupled experimental, analytical and numerical investigations were performed. Flexural and direct tension tests were first conducted to experimentally characterize material behavior. Following experimentation, a micromechanically-based analytical model was utilized to calculate the material's tensile failure response, which was compared to the experimental results. Lastly, to investigate the relationship between the tensile failure and flexural response, a numerical analysis of the flexural experiments was performed utilizing the experimentally developed tensile failure function. Results of the experimental, analytical and numerical investigations are presented herein.

## 1. Introduction

As part of the continued development of new and innovative construction materials for applications in civil, structural, and military engineering, high performance concrete has been maintained as an area of directed focus. Advancements in the science and technology of cementitous materials have brought about mesoscale to sub-microscale material engineering (through development of concepts such as particle packing theory, macro-defect free concrete, heat and pressure treatment to facilitate molecular structure manipulation, and microfiber inclusion to inhibit growth and localization of microcracks), and have resulted in materials with unconfined compressive strengths as high as 200 MPa or greater (O'Neil *et al.* 2004, Chanvillard and Rigaud 2003, O'Neil *et al.* 1999). High-strength concrete, with compressive strengths of 70 MPa and greater, and ultra-high-strength concrete (UHSC), with compressive strengths of 140 MPa and greater, have experienced continued growth in commercial application as the community's state of knowledge and production capability have advanced (Ngo *et al.* 2005, Bindiganavile *et al.* 2002, Shah 1997).

In conjunction with enhancement of unconfined compressive strength, significant research has been conducted to develop means of improving the tensile characteristics of cementitous materials. The classical approach of incorporating discrete reinforcing steel has been augmented with the

---

\* Corresponding author, Ph.D., E-mail: michael.j.roth@usace.army.mil

capability to reinforce with other, more advanced, materials such as ultra-high-strength steel meshes (3.2 GPa or greater), fiber-reinforced plastics, carbon-fiber strands, glass-fiber strands, and other high-strength and/or high-ductility fibers such as continuous aramid or polypropylene strands (ACI Committee 549 2004, ACI Committee 544 1996). A significant portion of this research on advanced reinforcement has focused on continuous strand applications. However, research has also been conducted on the inclusion and effect of discontinuous reinforcement.

Discontinuous reinforcement, consisting of short randomly distributed fibers, has been studied experimentally, analytically, and micromechanically with regard to its influence on concrete's tensile characteristics (Banthia and Gupta 2004, Giaccio and Zerbino 2002, Balaguru *et al.* 1992). Considering that individual fiber lengths may be as small as 12.5 mm, and fiber diameters may be as small as 0.5 mm or less, from a macroscopic viewpoint the fibers might be considered as a basic constitutive component of the concrete (in contrast to the typical discrete treatment of deformed bars or continuous strand reinforcement). However, with refinement in scale the fibers have been studied explicitly in terms of their interaction with the cementitous matrix (Li and Wang 2006, Nelson *et al.* 2002, Kanda and Li 1999, Li and Stang 1997, Li *et al.* 1996, Maalej *et al.* 1995, Li *et al.* 1993, Li 1992). Although this has resulted in new knowledge on the fiber/matrix interaction process, the stochastic nature of fiber dispersion, concentration, and orientation has still generally necessitated macroscale homogenization of their influence on a concrete member's global response to load. Only in more recent research have numerical models been developed to directly consider discontinuous fiber influence at the sub-macroscopic level (Beghini *et al.* 2007, Kabele 2002, 2003, 2004, 2007), but they have not been made applicable to widespread community use.

The focus of this research project was on a new ultra-high-strength, glass fiber-reinforced concrete (UHS-GFRC) material which was jointly developed by the U.S. Army Engineer Research and Development Center (ERDC) and the United States Gypsum Corporation (USG). The UHS-GFRC was developed for various military engineering applications, with the material development research jointly focused on (a) the generation of specific hardened properties, while (b) maintaining the necessary fresh material properties to facilitate commercial production. Typical application of the UHS-GFRC material was in the form of thin panels (approximately 12.7 mm in thickness) with various facings laminated to the surface. In consideration of this, the purpose of this research was to study the flexural and tensile properties of the panel's 12.7-mm-thick UHS-GFRC core. More specifically, objectives of the research included,

• Experimental investigation of the UHS-GFRC panel's flexural and tensile properties by means of third-point bending tests and direct tension tests,
• Application of published micromechanical models to analytically study the fiber/matrix interaction and its influence on macroscale material response, and
• Numerical modeling of the flexural material response utilizing the ABAQUS code (ABAQUS 2005).

## 2. UHS-GFRC specimens

To generate the desired material properties (fresh and hardened), a novel mixture composition was developed utilizing a blend of fine aggregate, cementitous and pozzolanic materials with a very low water-to-cement ratio of approximately 0.25. Details of the mix design are a proprietary development by ERDC and USG and therefore are not reported. However, basic constitutive components included foundry sand, Portland cement and silica fume with particle sizes ranging from approximately 0.5

mm to 0.1 microns, along with a high range water reducing admixture to facilitate workability in the production process. No materials with particle size greater than 0.5 mm were used in the mixture.

To generate the target unconfined compressive strength of 138 MPa or greater, prior research indicated the need for a special curing process which included a 7-day standard wet cure followed by a 4-day hot water bath and a 2-day oven cure. However, it was found that this curing protocol was not supportive of continuous-process production utilizing USG processing facilities. Therefore, through laboratory experimentation, USG researchers determined that with modifications to the material mix design the target strengths could be achieved with a typical 28-day moist cure protocol. The resulting mixture composition and 28-day curing process were subsequently adopted for production of the UHS-GFRC panel core. Unconfined compression strength testing conducted on 50-mm cube specimens (ASTM C 109-07), indicated average compressive strength and density measurements for the material of approximately 142 MPa and 2.3 g/cc, respectively.

Due to requirements for the Army program and the USG production-line processing, it was determined that continuous reinforcement in the form of strands, deformed wire, wire meshes, etc., would not be used. Rather, reinforcement was provided in the form of discontinuous fibers which could be efficiently incorporated into the production process. Although many types of fibers have been studied for use as discontinuous reinforcement in cementitous materials, alkali-resistant glass fibers were selected for this application based on prior experience with the material and efficiency in the production process.

Alkali-resistant glass fibers used in the material were AR2500 H-103 fibers produced by Nippon Electric Glass Company, and were incorporated at an approximate loading rate of 3 percent by volume. The fibers were chopped to an approximate 25.4-mm length and were kneaded into successive lifts of the cementitous material along the production line. From the manufacturer's specifications, properties of the glass fibers were as follows.

• Density: 2.7 g/cc
• Tensile strength: 1,270 to 2,450 MPa
• Elongation at break: 1.5 to 2.5%
• Young's modulus: 78.6 GPa
• Cross sectional area: 0.74 mm$^2$

As is typical for glass strand reinforcement, the individual AR2500 glass fibers were actually a glass fiber roving which was composed of glass strands and filaments. From the manufacturer's literature, a typical fiber, i.e., roving, consisted of 28 glass strands wound together, and each glass strand was composed of 200 glass filaments with a diameter of approximately 13 microns each. Resultantly, each glass fiber or roving actually included approximately 5,600 glass filaments. As will be discussed later, this makeup creates a complex set of fiber/matrix interaction conditions and results in challenges for the development of an accurate micromechanical model.

## 3. Flexural and direct tension experiments

Other ERDC researchers have experimentally determined the mechanical properties of UHSC materials under compression loading (Akers *et al.* 1998, Williams *et al.* 2009). However, far less work has been done to study its tensile characteristics, especially when reinforced with discontinuous fiber reinforcement. Therefore, an objective of this research was to conduct two series of laboratory

experiments to determine characteristic properties of the UHS-GFRC using flexure and direct tension tests. The first experimental series consisted of 10 closed-loop, third-point bending experiments performed to determine the load-displacement response of a specific panel configuration, as well as to determine the initial flexural modulus and first-crack strength of the material. Following the flexure experiments, a limited set of direct tension experiments were conducted. These were used to determine initial tensile modulus and first-crack strength for comparison to the flexural test results, as well as to determine the strain softening response of the material during failure. The strain softening response (in the form of a tensile stress versus crack opening function) could in-turn be used for comparison to micromechanical model results and as a tensile failure definition in a numerical constitutive model.

## 3.1. Flexural experiments

Flexural tests were conducted in accordance with ASTM C 947-03 on an MTS 810 testing machine. The MTS machine was configured with a 489-kN load cell and a linear variable displacement transducer (LVDT) monitored loading head. The loading system and LVDT were connected in a closed-loop manner, which provided displacement rate control in accordance with the ASTM standard. For all 10 tests, the displacement rate was set to 1.3 mm/min., corresponding to the minimum ASTM recommended rate.

The specimen support device was configured to provide a span of 910 mm between supports, and continuous strip loads were applied to the specimens 303 mm from each support. Test specimens were obtained from 760-mm by 1,220-mm panels produced on the USG production line. To
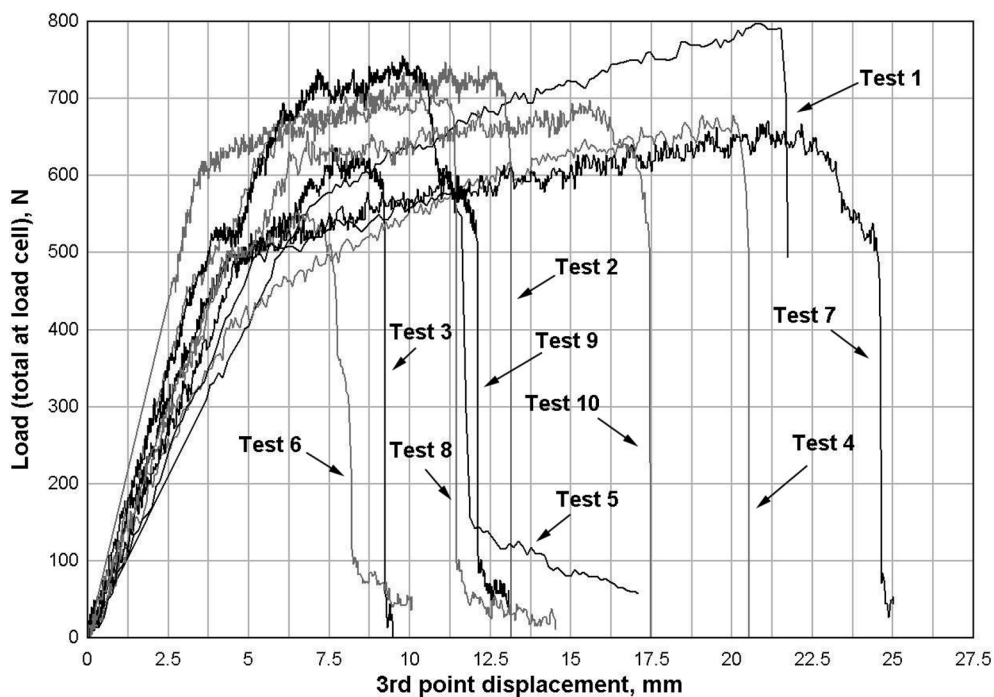


Fig. 1 Flexural test load versus third-point displacement results

Table 1 UHS-GFRC mechanical properties (flexural tests)

| Property | Mean | Standard deviation | CoV, % |
|---|---|---|---|
| Specimen thickness, $d$ (mm) | 11.8 | 0.9 | 7.6 |
| First crack load, $P_{fc}$ (N) | 502 | 58 | 11.5 |
| Ultimate load, $P_u$ (N) | 676 | 76 | 11.2 |
| First crack displacement, $\delta_{fc}$ (mm) | 4.5 | 1 | 22.2 |
| Ultimate displacement, $\delta_u$ (mm) | 13.7 | 5.3 | 38.6 |
| First crack strength, $\sigma_{fc}$ (MPa) | 13.0 | 2.1 | 16.1 |
| Initial flexural modulus, $E_{int}$ (GPa) | 39.2 | 7.6 | 19.4 |
| Post first crack modulus, $E_{pfc}$ (GPa) | 5.4 | 2.3 | 42.6 |

accommodate space limitations on the MTS machine, 250-mm by 1,020-mm test specimens were cut from the production line panels.

A summary of flexural test results is shown in Fig. 1. Shown are plots of the applied load (total load measured at the load cell) versus displacement at the third-points of the panels. As seen, the panels exhibited a generally bilinear response, with an initial linear response up to first-crack formation and then a second linearly increasing response until the point of ultimate failure. In some cases the panels exhibited a small residual load capacity after ultimate failure, as seen for Tests 6, 7, 8, and 9. In these cases, the bridging fibers did not completely fail, i.e., rupture or pull out from the cementitous matrix, during macrocrack formation at ultimate load. The remaining fibers generated a small amount of residual tensile resistance in the cross section, providing the residual flexural capacity observed for these specimens.

From the test data, mechanical properties and load-response characteristics were determined and are summarized in Table 1. Shown are mean values, standard deviations and coefficients of variation (CoV) for flexural modulii, flexural strength at first-crack, load and displacement values at first-crack and ultimate load, and thickness of the cross section at the crack face.

In Table 1, flexural modulus, $E_{int}$, and the first-crack strength, $\sigma_{fc}$, were calculated from the simple elastic flexure expressions given in ASTM C 947-03, which are repeated in Eqs. (1) and (2) below.

$$E_{int} = \frac{5P_{fc}L^3}{27\delta_{fc}bd^3} \qquad (1)$$

$$\sigma_{fc} = \frac{P_{fc}L}{bd^2} \qquad (2)$$

In these expressions, $L$ is the specimen span (910 mm) and $b$ is the specimen width (250 mm) (other variable definitions given in Table 1).

In consideration of the panels' bi-linear response, flexural modulus was also calculated for the post first-crack response phase. The expression for post first-crack modulus, $E_{pfc}$, is given in Eq. (3), and was derived using the same elastic flexure expression given in Eq. (1).

$$E_{pfc} = \frac{5(P_{fc}-P_u)L^3}{27(\delta_{fc}-\delta_u)bd^3} \qquad (3)$$

When utilizing Eq. (3) to determine the post first-crack modulus, it is acknowledged that the

fundamental assumptions of simple elastic flexure are no longer fully met. Namely, the assumption of material homogeneity is not completely satisfied due to microscale damage within the matrix, which initiated at the first-crack load. However, because damage formation initially occurred at the microlevel as distributed microcrack formation and growth (coalescing to a single macrocrack at the ultimate failure point), at the macroscale the material was still viewed as a homogeneous medium with reduced stiffness. The reduced stiffness was a result of the change in microstructure conditions within the matrix.

Shown in Table 1, the mean initial modulus was determined to be 39.2 GPa with a CoV of 19 percent. As expected, the post first-crack modulus was significantly less, with nearly an order of magnitude reduction to 5.4 GPa. Mean first-crack strength was determined to be 13 MPa, which was reached at a load of approximately 502 N. The second phase of response exhibited a moderate amount of deflection hardening, with an approximate 26 percent load increase from the first-crack load to the mean ultimate load of 676 N. Greatest variability in the test results was observed in the post first-crack modulus and displacement at ultimate failure, with CoV's of 38.6 percent and 42.6 percent, respectively. The significant variability in post first-crack response was attributed to a variable distribution of fibers within the panels. In some cases, such as Test 7, a sufficient quantity of bridging fibers were present at the crack location to achieve a maximum displacement of approximately 25 mm, while in Test 6 far fewer fibers were present to inhibit macrocrack formation and panel failure (resulting in ultimate failure at a displacement of approximately 7.5 mm). The observance of this variability highlights the stochastic nature of fiber distribution in the material, and indicates that the assumption of uniform fiber distribution throughout the matrix may not be appropriate in many cases.

### 3.2. Direct tension experiments

In conjunction with the flexural tests, a limited number of direct tension tests were performed to investigate material response under pure tension loading. Four specimens were tested, two of which failed prematurely. Subsequently, the remaining test results were not sufficient to establish a statistically complete description of the material's direct tension response. However, the data were used as initial findings, which should be followed with additional direct tension tests to verify results.

In contrast to the flexural experiments, which followed a published ASTM standard test method, standardized procedures were not available for design and execution of the direct tension tests. In the literature, it was noted that a U.S. standard has not been developed for this type of test, presumably because of the significant difficulty in obtaining a pure tensile loading condition. Furthermore, the convolution of strain localization in a cracked concrete specimen further increases the difficulty in extracting meaningful strain data from a test, which is also a likely cause for the lack of standardized tests of this type.

Although standard test methods were not available, research pertaining to concrete direct tension tests has been documented (Zheng *et al.* 2001, Wang *et al.* 1990). From these works, the approach and procedures used for these tests were developed so that they would reasonably follow other published efforts.

Direct tension experiments were conducted with the same MTS 810 test machine as used in the flexural tests. The tests were conducted using closed-loop displacement-rate control, with a loading head displacement rate of 0.25 mm/min. Because of the relatively brittle response expected for the material, even with inclusion of the reinforcing fibers, foil strain gages were utilized to document

specimen deformation. Strain gages were selected because of their capacity to gather high resolution data during the tensile straining, fracture and failure process. However, this also necessitated the use of notched specimens to determine the failure location *a priori* so that the strain gages could be appropriately placed.

In the same manner as done for the flexural tests, specimens used in the direct tension tests were cut from larger, nominally 12.7-mm-thick panels produced from the USG production line. In consideration of the need for notched specimens, a shape was selected which provided a v-shaped notch on both edges of the specimen (Fig. 2). Overall length of the specimens was 254 mm, and overall width was 76.2 mm. The v-notch was located at the specimen center and tapered over a distance of 38.1 mm. At the notch tip, the specimen width was reduced to 50.8 mm.

To document specimen deformation, six 25.4-mm-long foil strain gages were attached to the specimens. The gages were manufactured by Vishay Micro-Measurements, Inc., and were type 10CBE-350/E. Three gages were attached to each side of the specimen, one centered between the notch tips and the other two located 63.5 mm from each end. All gages were oriented to measure strain in the direction of the applied load. The strain gage locations are shown in Fig. 2, along with the notation scheme used to identify the gages (*A*1, *A*2, *A*3). Note that gages on the opposite side of the specimen were similarly identified as *B*1, *B*2 and *B*3.

To connect the specimens to the MTS machine, steel end caps with threaded fasteners were used. The caps were epoxied to the specimen ends and were rigidly connected to the test machine. Use of rigid connections was expected to promote uniform crack opening width across the specimen, instead of allowing the crack width to grow non-uniformly (from one side of the specimen to the other) as occurs with non-rigid connections.

Analysis of the test results was performed in two stages. First, the pre-crack response was analyzed to determine the material's initial elastic response characteristics under a pure tension load. In this analysis step, only data from the *A*1/*B*1 and *A*3/*B*3 gage pairs were utilized to avoid complications arising from stress concentrations in the notch zone. Following analysis of the initial elastic response, a second analysis was performed to determine the first-crack strength and the post-
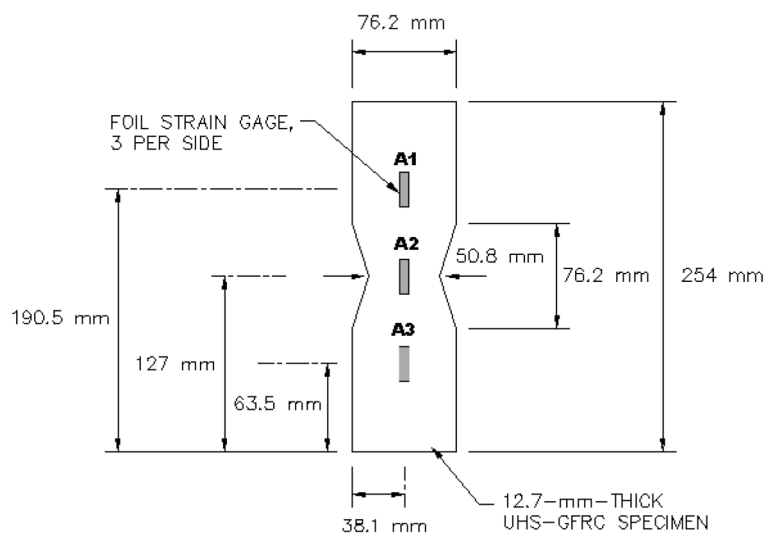


Fig. 2 Direct tension test specimen (without steel end caps)

crack tensile stress versus crack width function. Because specimen failure was localized to the notch location, only data from the *A2/B2* pair was used in the second analysis phase.

Prior to analyzing data from either the pre- or post-crack response, a finite element (FE) analysis was conducted to investigate the influence of specimen shape on the stress state at the strain gage locations. The FE analysis was performed using ABAQUS, and was limited to a linear elastic analysis using a simple isotropic, elastic constitutive law. Justification for use of the simple material model was based on the fact that the analysis' purpose was to consider stress state conditions prior to crack initiation, not to study the specimen response during failure. For the material definition, Young's modulus and Poisson's ratio were specified as 39 GPa and 0.23, respectively. Young's modulus was taken from results of the flexural tests, and Poisson's ratio was based on results from a prior ERDC study on a similar material (Akers *et al.* 1998). The model was meshed with linear, 8-noded hexahedral elements (ABAQUS element type C3DR8), which possessed 3 degrees of freedom per node. Using the hexahedral elements, an *h*-refinement analysis was conducted to evaluate mesh dependency of the calculated stress state at the gage locations. Element size (through the thickness of the specimen) was varied from 6 mm to 1 mm, and results indicated that the stress conditions reasonably converged with an element size of approximately 2.5 mm. Therefore, an element thickness of 2.5 mm was used, providing five elements through the specimen thickness. With the given mesh, the model contained 26,390 elements, 32,940 nodes, and 98,820 degrees of freedom.

Results from the FE analysis with an applied end load of 4,900 N (approximate peak load applied in the direct tension tests) are shown in Fig. 3. Internal stress conditions at the *A*1 and *A*2 gage locations are noted in the figure. As seen, the computed internal stress at gage *A*1 was 5.3 MPa. Calculating the engineering stress from total load divided by initial cross-sectional area at the gage (yielding a stress level of 5.05 MPa), the FE analysis indicated that stress at the *A*1 gage location was approximately 5 percent greater than the engineering stress.

Utilizing stress conditions calculated from the FE model, coupled with strain measurements from
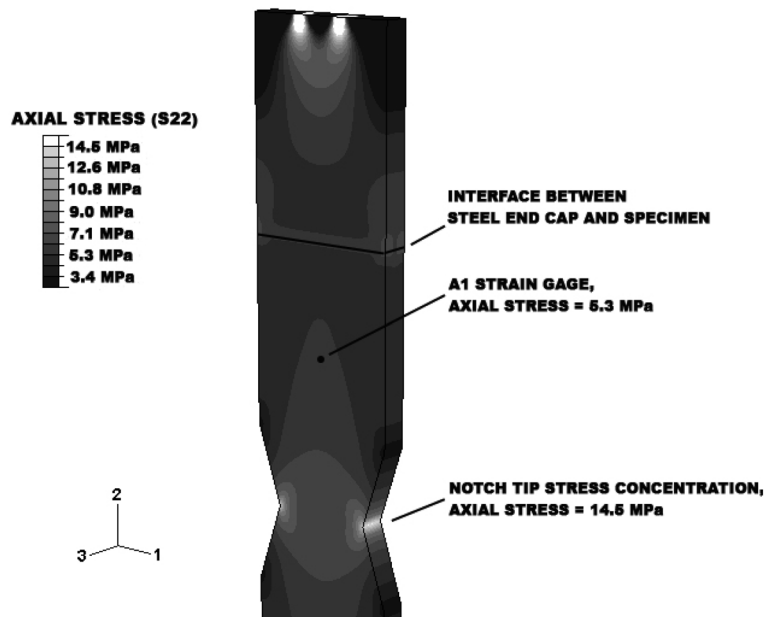


Fig. 3 FE calculated stress state in direct tension specimen (applied load = 4,900 N)
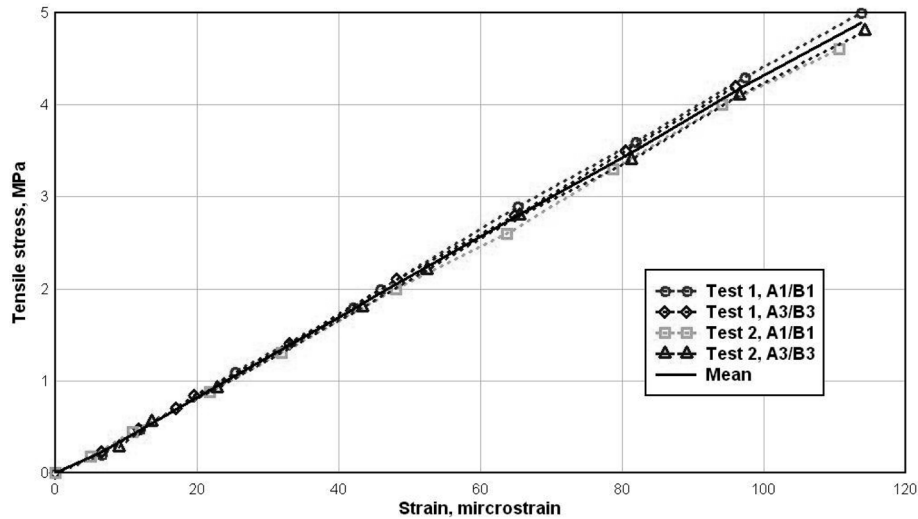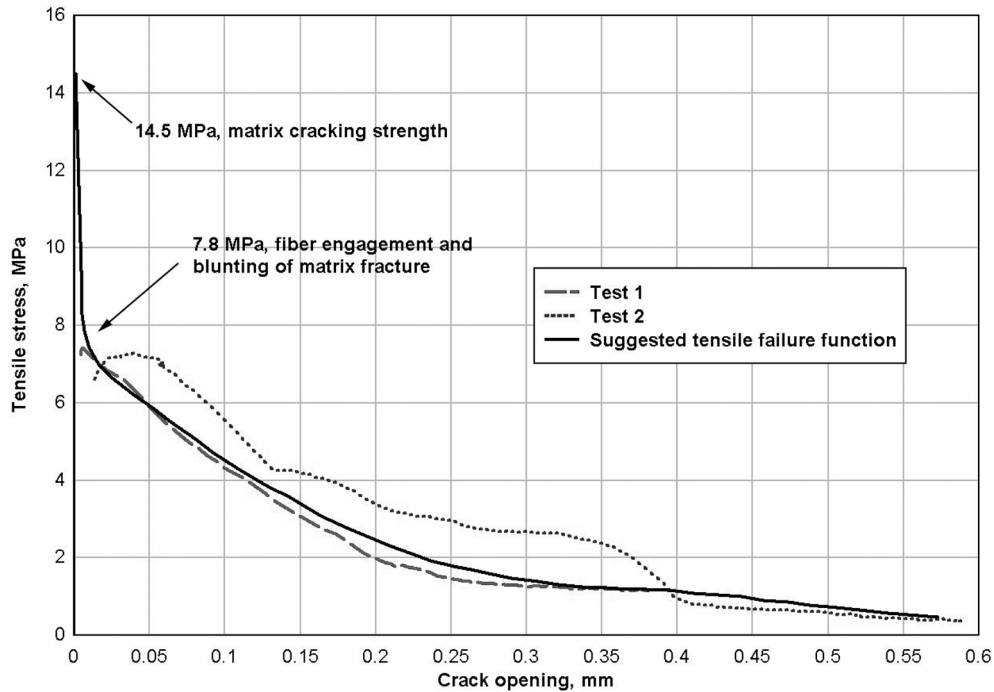
Fig. 4 Direct tension tests, pre-crack stress-strain response

the direct tension experiment, pre-crack stress-strain response of the tension specimens at the *A1/B1* and *A3/B3* locations are shown in Fig. 4. From the figure, relatively uniform linear response was observed at all gage locations. Mean response was calculated from the four data sets, and the initial elastic modulus of the direct tension specimens was calculated to be 43 GPa. This was approximately 10 percent greater than the initial modulus of 39 GPa determined from the flexural tests.

Following analysis of the specimens' pre-crack response, the second analysis phase focused on the cracking strength and the post-crack tensile stress versus crack opening width relationship ($\sigma$-$\delta$ function) for the material. From the experimental data, peak applied loads at crack initiation (which occurred at the notch tip) were 4,970 N and 5,000 N in Tests 1 and 2, respectively. Utilizing engineering stress definition at the notched section, cracking strength of the material was calculated as approximately 7.8 MPa. However, this neglected the notch tip stress concentration, which was the driving stress for crack initiation. Referring back to Fig. 4, the FE analysis indicated that notch tip stresses were approximately 14.5 MPa at peak load, or approximately 1.8 times greater than the engineering stress at the notched section. Therefore, utilizing peak loads from the direct tension experiment and stress concentration at the notches determined from the FE analysis, tensile strength from the direct tension experiments was estimated to be approximately 14.5 MPa, which was 12 percent greater than the $\sigma_{fc}$ (13.0 MPa) determined from the flexural experiments.

In addition to tensile strength, an estimate of the $\sigma$-$\delta$ function was desired from the direct tension data. In Fig. 5, $\sigma$-$\delta$ functions from Test 1 and Test 2 are given. Note that the data has been truncated to remove the pre-crack response, as it was not the focus of this portion of the data analysis. The curves were calculated as a mean of the *A2/B2* pair strain data, where strain was converted to crack opening based on the assumption that all strain measured after the peak strength was localized to the crack location. It is recognized that this assumption was not fully valid during the initial crack propagation due to characteristic length effects. However, the assumption was deemed sufficient for the purposes of this analysis.

Tensile stress in Fig. 5 was calculated based on the engineering stress definition, using total applied load and the specimen gross cross section at the notch. This stress definition was used

Fig. 5 Direct tension tests, $\sigma$-$\delta$ functions

because the $\sigma$-$\delta$ function was expected to be a representation of the averaged effect of all fibers bridging at the notched section, which would tend to correspond with the engineering stress definition. Although the engineering stress expression was assumed appropriate based on the preceding argument, the tensile cracking strength, which initiated the failure process at the notch tips, is neglected. Therefore, in Fig. 5 a suggested tensile failure function is also shown. The suggested tensile failure function augments the test data with the crack initiation strength of 14.5 MPa. Meaningfulness of this stems from the suggestion that on reaching the matrix cracking strength of 14.5 MPa, the fracture process was initiated at a notch tip and immediately progressed through the section. As this occurred, the glass fibers were engaged to inhibit the cracking failure, providing a maximum fiber bridging strength of approximately 7.8 MPa at the cracked section. As the crack width subsequently increased, the fibers progressively failed through pull out and rupture, eventually losing all tensile resistance at the crack.

## 4. Micromechanical model analysis

After completing the experimental characterization, the second research objective was to explicitly consider interaction between the fibers and cementitous matrix and investigate how material interactions at the mesoscale influenced material response at the macroscale. To accomplish this, a series of micromechanical models developed by V.C. Li and others (Maalej *et al.* 1995, Li *et al.* 1993, Li 1992, Li *et al.* 1991) were used to calculate the strain softening response of the UHSC-GFRC material. The micromechanical models utilize a progressive approach to first analytically

describe the behavior of a single fiber pulled from a cementitous matrix, and then extend the model formulation to estimate the tensile response of a cementitous composite reinforced with randomly distributed fibers. The primary outcome is derivation of a tensile stress versus crack opening function for a specific material, similar to the $\sigma$-$\delta$ function experimentally measured in the direct tension experiments.

## 4.1. Single fiber pullout response

To formulate the micromechanically-based, analytical procedure for determination of a fiber reinforced concrete's macroscale tensile response, a foundational model is first adopted to describe the basic fiber and concrete matrix interaction (Li *et al.* 1993, Li 1992, Li *et al.* 1991). The model is based on a single discontinuous fiber embedded in a cementitous matrix, with the fiber oriented normal to the surface of the crack plane. It is initially assumed that the fiber tensile strength is sufficient to prevent rupture under tensile load, and therefore the failure mode is pullout from the cementitous material. It is also assumed that the fiber has a finite embedment length, $L_{embed}$, such that when it is loaded with an axial load, $P_f$, an interface stress, $\tau_{if}$, is developed. The interface stress is maximum at the crack face and decays over the finite fiber length. As the tensile load is increased, the interface stress will eventually reach the bond strength between the fiber and the cementitous matrix, $\tau_{if\max}$, and a slip-plane will form along the fiber length. Once the maximum interface stress has progressed to the fiber tip, the slip-plane will fully form and the fiber will begin to pull out of the matrix. The phase of fiber response up to the point of full slip-plane formation is referred to as the debonding phase, and is generally characterized by a stiff, positive slope response in a load versus crack opening plot. After full debonding has occurred, the second phase of response (known as the pullout phase) is initiated, which continues until the fiber is completely pulled from the matrix. These typical response phases are shown in Fig. 6 (a).

Basic expressions for the single fiber response to loading are given in Eqs. (4) through (6). Note that these equations are accompanied with the assumptions that the fiber bond mechanism is fully frictional, $\tau_{if\max}$ is constant, and tensile strength of the fibers is sufficient to prevent rupture during the pullout process.

$$P_f(\delta) = \pi \sqrt{\frac{E_f d_f^3 \tau_{if\max} \delta}{2}} \text{ for } \delta \leq \delta_0 \tag{4}$$

$$P_f(\delta) = \pi \tau_{if\max} L_{embed} d_f \left(1 - \frac{\delta - \delta_0}{L_{embed}}\right) \text{ for } \delta_0 \leq \delta \leq L_{embed} \tag{5}$$

$$\delta_0 = \frac{2 L_{embed}^2 \tau_{if\max}}{E_f d_f} \tag{6}$$

In these expressions, $\delta$ is the crack opening generated by an applied tensile load, $\delta_0$ is the crack opening width at end of the debonding phase, $E_f$ is the fiber elastic modulus and $d_f$ is diameter of the fiber. From evaluation of Eqs. (4) through (6), it is seen that the basic fiber pullout model is simply a function of basic fiber properties ($E_f$ and $d_f$), embedment of the fiber ($L_{embed}$), and the contact surface between the fiber and the matrix (described by $\tau_{if\max}$).

The fiber properties and embedment conditions can be readily defined, referencing the previously stated fiber properties and using an embedment length of 12.7 mm for the 25.4-mm-long fibers.

(a) Single fiber pullout response



(b) Composite bridging stress versus crack opening



(c) Composite bridging stress versus crack opening (augmented with matrix cracking strength)
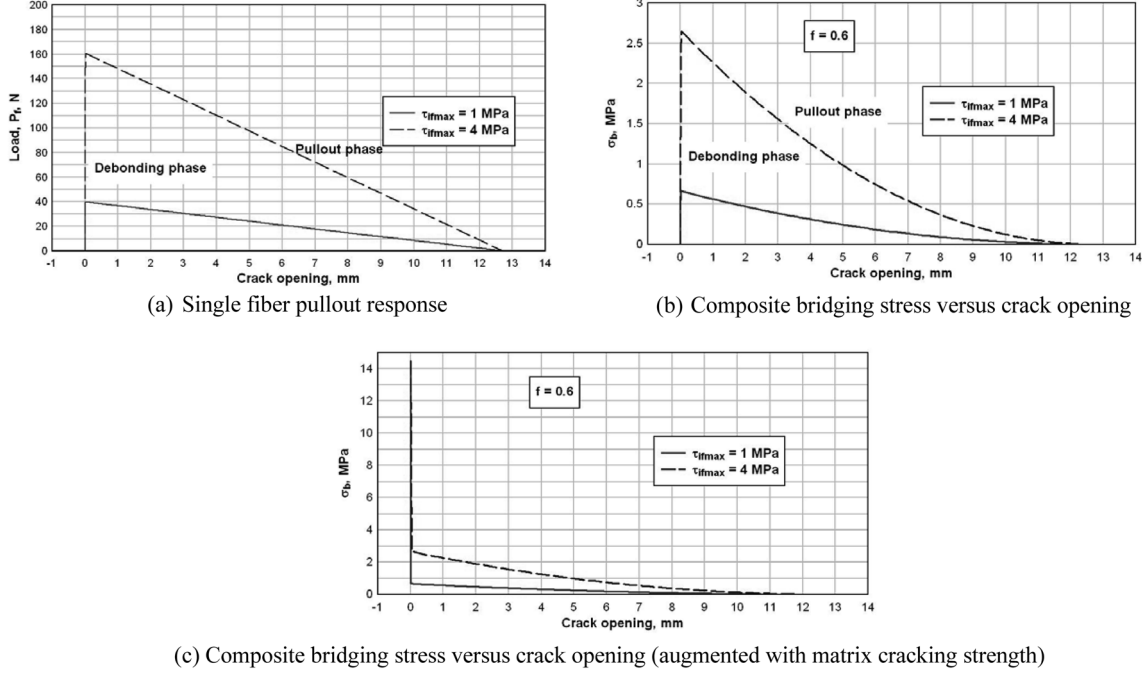
Fig. 6 Micromechanical model, UHS-GFRC tensile failure function

Therefore, the remaining property which must be defined is the interface condition between fiber and matrix, which is a significant parameter in the micromechanical model development. Interface bond strength is typically determined from fiber pullout experiments, where a single fiber is pulled from the cementitous matrix. However, single fiber pullout experiments were beyond the scope of this study. Therefore, other works were reviewed to determine an estimate of the interface bond characteristics, which were summarized in Roth (2008). Although interface bond characteristics were reported for a number of fiber types with a wide range of interface strengths (ranging from 0.05 MPa for nylon fibers to 37.9 MPa for PVA fibers), no data was found for glass fibers. Therefore, an initial bounding estimate of 1 MPa to 4 MPa was made for $\tau_{ifmax}$, which disregarded the limit strengths reported for nylon and PVA materials. An example of the single fiber pullout model evaluated with the glass fiber properties and interface bond strengths of 1 MPa and 4 MPa is given in Fig. 6(a).

### 4.2. Single fiber pullout, fiber inclination effects

After developing the single fiber model with the assumption of fiber orientation normal to the crack surface, the influence of fiber orientation angle was considered (Li 1992). To account for the effect of fiber orientation angle with respect to the crack surface (during both the debonding and pullout phases), Eqs. (4) and (6) are modified as shown in Eq. (7).

$$P_f(\delta, \phi) = P_f(\delta)e^{f\phi} \tag{7}$$

In Eq. (7), $f$ is termed the snubbing coefficient and $\phi$ defines the angle between the fiber and crack face. Because $\phi$ defines the fiber orientation angle, it is specified over a range of 0 radians to 1.5708

radians. The snubbing coefficient defines interface conditions between the fiber and matrix as the fiber is bent at the crack face. Since $f$ is dependent on interface properties between the fibers and the matrix, it must also be determined experimentally, similar to the frictional bond strength. Because determination of the snubbing coefficient was also beyond the scope of this study, reference was again made to the literature for coefficient estimates associated with various fiber types, which are summarized in Roth (2008). Similar to $\tau_{if\max}$, no data was found for glass fiber snubbing coefficients, and therefore a value between 0.6 and 0.8 was assumed from the reported data.

Considering Eq. (7), it is seen that the correction factor, $e^{f\phi}$, for the single fiber load versus displacement function is a constant for any given inclination angle and snubbing coefficient. Therefore, the effect is to simply shift the debonding and pullout response curves so that the pullout load, $P_f$, required for a given crack opening, $\delta$, increases as the orientation angle and/or snubbing coefficient increase.

### 4.3. Composite material response model

Utilizing Eqs. (4) through (7) to describe the response of a single fiber when oriented normal and at angle to a crack, it is next required to consider the stochastic nature of fiber positioning and orientation with respect to the crack surface. Probability density functions are used to describe the random fiber distribution (Li *et al.* 1993), and are given as follows.

$$p(\phi) = \sin(\phi) \tag{8}$$

$$p(z) = \frac{2}{L_f} \tag{9}$$

In these expressions, $p(\phi)$ describes the probability of fiber orientation angles for values of $\phi$ between zero radians and 1.5708 radians, $p(z)$ describes the probability of fiber embedment lengths for values of $z$ between zero and one-half the fiber length, $z$ is given as the distance from centroid of the fiber to the crack face, and $L_f$ is the fiber length. Note that in the application of Eq. (8) it is assumed that the fibers are uniformly distributed throughout a three-dimensional matrix. However, in this case due to thickness of the 12.7-mm-thick panels the assumption of three-dimensional uniformity may not be fully applicable–with the fibers having preferential orientation in a two-dimensional plane.

Based on the probability density functions and single fiber pullout model, the bridging stress versus crack opening relationship for a cementitious matrix reinforced with randomly distributed fibers is given in Eq. (10) (Li *et al.* 1993).

$$\sigma_b(\delta) = \frac{4V_f}{\pi d_f^2} \int_{\phi=0}^{\phi \neq \pi/2} \int_{z=0}^{z=(L_f/2)\cos\phi} P_f(\delta, z, \phi) p(\phi) p(z) dz d\phi \tag{10}$$

In Eq. (10), $\sigma_b(\delta)$ is the composite bridging stress at a crack surface and $V_f$ is the volume fraction of fibers in the matrix. $P_f(\delta, z, \phi)$ is defined as the axially applied load for a single fiber as a function of (a) crack opening, (b) fiber centroidal distance from the crack surface, and (c) fiber orientation angle. Expressions for $P_f(\delta, z, \phi)$ during the debonding and pullout response phases are given in Eqs. (11) and (12), respectively.

$$P(\delta, z, \phi) = \frac{\pi}{2}(\sqrt{(1+\eta)E_f d_f^3 \tau_{if\max}\delta})e^{f\phi} \text{ for } \delta \leq \delta_l \tag{11}$$

$$P(\delta, z, \phi) = \pi \tau_{if_{\max}} L_{embed} d_f \left(1 - \frac{\delta - \delta_1}{L_{embed}}\right) e^{f\phi} \quad \text{for } \delta_l \le \delta \le \delta_l + L_{embed} \tag{12}$$

$$\eta = \frac{V_f E_f}{V_m E_m} \tag{13}$$

$$\delta_1 = \frac{4 L_{embed}^2 \tau_{if\max}}{(1 + \eta) E_f d_f} \tag{14}$$

In Eq. (13), $V_m$ and $E_m$ are the volume fraction and modulus of the matrix, respectively. $\delta_l$ describes the crack opening width at which all fibers within the matrix have debonded and only pullout resistance remains, similar to $\delta_0$ for the single fiber expressions. Closed-loop expressions for the composite bridging stress have also been derived by Li *et al.* (1993), which are based on the relationships given in Eqs. (11) and (12).

Utilizing the composite bridging stress expressions and parameters for the UHS-GFRC material, the composite bridging stress versus crack opening relationships were calculated for $\tau_{if\text{max}}$ of 1 MPa and 4 MPa, and are given in Fig. 6(b). From the figure it is seen that for the case where $\tau_{if\text{max}}$ was equal to 1 MPa, the fiber debonding process was initiated and continued until a peak bridging strength of approximately 0.6 MPa was achieved. Similarly, with $\tau_{if\text{max}}$ equal to 4 MPa a peak bridging strength of 2.7 MPa was reached. In both cases, at peak strength the fibers fully debonded and pullout failure was initiated. Because of the random fiber dispersion, strength decay during the pullout process was non-linear, continuing until all fibers had pulled from the matrix at a maximum crack opening width of approximately 12.7 mm. Magnitude of the maximum crack opening width was a natural result of the assumption of uniform fiber dispersion in the matrix (and subsequent use of the probability density function $p(z)$), where it was assumed that fiber embedment uniformly ranged from zero to $L_{embed}$, or one-half of the fiber length. As a result of this assumption and because fiber rupture was not considered in this form of the bridging stress model, tensile resistance only reached zero when the crack opening reached 12.7 mm (corresponding to the maximum fiber embedment length).

An important observation from implementation of the composite bridging stress model is that it does not take into consideration the matrix cracking strength. Rather, the model is initiated with the assumption that a crack has formed in a cementitous matrix, which is bridged by a random distribution of reinforcement fibers. With this as the initial condition, bridging stress increases from zero to some peak value, corresponding to the maximum bridging strength which can theoretically be achieved with the given fiber/matrix interaction. After reaching maximum strength, the model calculates strength decay during fiber failure at the crack, as shown in the figure.

In consideration of the preceding observation, to fully describe tensile failure in the cementitous composite it is necessary to augment the micromechanical model results with cracking strength of the cementitous matrix. In doing this, it is implied that first the matrix reaches it's tensile fracture strength, at which point a crack is formed in the material. Once matrix cracking occurs, the fibers become engaged and either provide additional tensile strength to the composite if the maximum fiber bridging strength is greater than the matrix strength, or a sharp strength loss occurs if the fiber bridging strength is less than that of the matrix. Taking the matrix fracture strength of the UHS-GFRC material to be approximately 14.5 MPa from the direct tension tests, the implication is that after matrix fracture a sharp strength loss occurs until the fiber bridging strength is reached and the

fibers become fully engaged.

Augmentation of the micromechanical model results with the matrix cracking strength is shown in Fig. 6(c). Because the plot is given in terms of tensile stress versus crack opening width, the matrix cracking strength of 14.5 MPa corresponds to a crack opening width of zero. The tensile stress immediately drops to the maximum fiber bridging strength of 0.6 MPa (2.7 MPa for $\tau_{if\text{max}}$=4 MPa), and then the calculated strength decay occurs until a crack opening width of 12.7 mm is reached. From comparison to the $\sigma$-$\delta$ function determined in the direct tension experiments (Fig. 5), it is noted that the fiber bridging strength from the micromechanical model is significantly lower than the strength estimated from the experiments. Furthermore, the maximum crack opening width determined from the model is much greater than that observed in the experimental data.

With respect to the fiber bridging strength, as seen in Eqs. (10) through (12) the maximum fiber bridging stress is primarily a function of the fiber characteristics and the fiber/matrix interface conditions. Since fiber properties used in the composite bridging model were based on manufacturer's published data, the initial assumption regarding interface bond strength was reconsidered. From re-evaluation of the composite bridging stress expressions with $\tau_{if\text{max}}$ equal to 12 MPa, maximum bridging strength for the fibers was found to be approximately 7.6 MPa. This was in much closer agreement with the experimental observations, and the resulting implication was that that the interfacial bond strength between the glass fibers and the high-strength matrix may be much higher than initially assumed.

In addition to the maximum fiber bridging strength, it was observed that maximum crack opening width calculated from the micromechanical model was significantly different than that measured in the experiments. As previously noted, the maximum crack opening width from the micromechanical model was based on the assumptions of (a) uniform dispersion of fiber embedment at the crack face (zero embedment to one-half of the fiber length), (b) pullout failure of the fibers, and (c) constant interface bond strength during the pullout process. With these assumptions, the model naturally predicts a maximum crack opening width of one-half the fiber length. However, not considered in this formulation of the model are the effects of fiber rupture (addressed in the following section) and variation of the interface conditions during the fiber failure process.

Other research has indicated that depending on fiber type, interfacial bond strength may not be constant with fiber displacement (Li and Stang 1997). Depending on fiber surface characteristics, the fibers may be abraded by the surrounding matrix (in the case of soft fibers) or may damage the matrix surface (in the case of hard fibers). The result is a change in the interface conditions between the fibers and the matrix, which yields either a slip-softening or slip-hardening variation in $\tau_{if\text{max}}$. In the case of the glass fibers, it has been noted that they may bring about a slip-softening effect due to smoothing of the matrix interface during pullout. It has also been noted that glass fibers may exhibit a telescoping effect during the pullout process. Recalling that the individual glass fibers are actually a roving of multiple strands and filaments, telescoping refers to a process where only the outer strands fully interact with the matrix, and the inner strands simply pullout of the fiber core as the crack width increases. The result of this telescoping process would be much sharper strength decay during the fiber failure process, in contrast to the type of response which would be observed for solid fiber materials such as steel. This considered, the effect of telescoping is qualitatively similar to the response observed in the experimental data and is a likely source of the significant difference in maximum crack opening width.

### 4.4. Composite material response model, fiber rupture effects

An initial assumption given for the single fiber pullout model was that the fibers were sufficiently strong to prevent rupture, resulting in a failure mode solely based on pullout. However, other research has documented fiber rupture failure modes for brittle materials such as glass and carbon (Maalej *et al.* 1995). Therefore, the potential for fiber rupture in the UHS-GFRC material was further considered.

To incorporate fiber rupture effects into the micromechanical model formulation, fiber rupture potential is expressed in terms of a failure envelope (Maalej *et al.* 1995), as given in Eq. (15).

$$L_u(\phi) = L_c e^{-f\phi} \tag{15}$$

$$L_c = \frac{\sigma_{fu} d_f}{4\tau_{if\,\max}} \tag{16}$$

In these expressions, $L_c$ represents the critical embedment length to initiate rupture in a fiber oriented normal to the crack surface and $\sigma_{fu}$ is the fiber ultimate tensile strength. From Eq. (15), the combination of embedment lengths and orientation angles that result in failure of a fiber can be determined based on the fiber properties (strength and size) and interfacial bond conditions, yielding a failure envelope, $L_u(\phi)$.

Utilizing the previously assumed fiber properties, the failure envelope was evaluated to determine the minimum interface bond strength required to initiate fiber rupture in the material. Performing this analysis, it was found that the minimum required bond strength to initiate rupture of the 25.4-mm-long fibers was approximately 14.5 MPa. Similarly, it was found that the bond strength required to rupture all fibers in the material was approximately 34.5 MPa. Based on these results, it was seen that to initiate fiber rupture the interface bond strength must be approximately 1.2 times greater the previously determined value (i.e., 12 MPa). Therefore, it was concluded that fiber rupture, at least in the form expressed in this model, did not significantly contribute to the composite material response.

## 5. Flexural FE model

The final research objective was to perform finite element analyses of the UHS-GFRC panels' flexural response. Purpose of the analyses was to study the relationship between the tensile failure function determined from the direct tension experiments and flexural response of the panels. In the study, ABAQUS was used to perform an implicit analysis of panel flexural response with the experimentally determined tensile failure function used as part of the constitutive model definition.

Four-noded shells with user-defined through-the-thickness integration points (ABAQUS element type S4R) were used to model the UHS-GFRC panels. Element dimensions were defined as approximately 12.7 mm by 12.7 mm, and the shell thickness was specified to be 11.8 mm, corresponding to the mean panel thickness, *d*, given in Table 1. Reduced integration was specified, and a stiffness approach to hourglass control was used. Based on the results of an investigation of model sensitivity to the number of integration points, nine through-the-thickness points were chosen, and Simpson's rule was specified as the through-the-thickness integration technique. Nine points can typically be used to reasonably model the progressive tensile failure of concrete through a given

section (ABAQUS 2004a). The overall panel model was 1,016-mm long by 127-mm wide. This discretization contained 810 elements, 902 nodes, and 5,412 degrees of freedom. Although the panel was modeled at one-half of the true width, i.e., 127 mm instead of 254 mm, results presented herein were scaled as appropriate for the full-size panel. Pin and roller boundary conditions were applied to the model, which provided a 910-mm span between supports. Strip loads were applied as surface tractions at the model third-points in accordance with the experimental setup.

Two constitutive models were used in concert in the analysis. The first was a simple elastic material model used to capture the initial linear response phase. The elastic model was coupled with a concrete damage plasticity model that is based on the works of Lubliner *et al.* (1989) and Lee and Fenves (1998) and was used to describe the UHS-GFRC's strain softening and ultimate failure. The damage plasticity model implements tension and compression damage through stiffness degradation, utilizes a plastic yield function with a non-associated flow rule, and implements viscoplastic regularization (ABAQUS 2004b). The material's initial elastic modulus was defined as 41 GPa, which was calculated from combined results of the flexure and tension experiments, and Poisson's ratio was defined as 0.23. Compressive failure and plasticity parameters used in the analysis are given in Roth (2008).

In the damage plasticity model, once a specified tensile failure stress is reached (denoting the limit of initial linear-elastic response), the material model follows a user-defined tensile stress versus cracking strain function, which in this case was taken from the direct tension test experimental data. To express the measured failure function in stress versus strain form, the suggested tensile failure curve shown in Fig. 5 was translated from crack width to cracking strain by "smearing" the crack width over the element length of 12.7 mm. For example, if the crack width was 0.1 mm, the strain value would be 0.008 by dividing the crack width by the element length. It is noted that this neglects the true effect of strain localization that occurs during concrete failure and the challenges associated with the use of finite elements to model concrete's tensile failure response. However, it was of interest to determine how well this simple model could be applied to the material.

The analyses were performed using the modified Riks method, which is a load-displacement-constraint solution method. In the Riks method, a load history is not prescribed. Rather, the model iteratively calculates the system's tangent stiffness at a current solution point, applies a load that is proportional to a reference load specified by the user, and uses a swinging-arc technique to find the load-displacement point of equilibrium. Although computationally more expensive, the advantage of the Riks method is that it allows for stable calculation of the panels' post-crack deflection hardening response and ultimate failure, unlike the Newton-Raphson technique.

Two FE analyses were conducted (labeled Model 1 and Model 2), the results of which are shown in Fig. 7. Model parameters for both of the analyses were the same with exception of the tensile failure definitions (Fig. 8) and the use of viscoplastic regularization. Viscoplastic regularization was used in conjunction with Model 1 because it was found that the sharp change in stiffness occurring at the point of fiber engagement (approximately 7.8 MPa) was too significant for solution convergence. Inclusion of viscoplastic regularization in the damage plasticity model assists in the convergence of softening problems during implicit calculations by regularization of the constitutive equations in accordance with the Duvaut-Lions regularization scheme (ABAQUS 2004b). Model 1 results were calculated with a viscoplastic regularization value of $1 \times 10^{-7}$.

As seen in Fig. 7, Model 1 results showed an excellent match to the panel's initial linear-elastic response. Furthermore, the model accurately calculated the sharp transition from initial system stiffness to the deflection-hardening response, which coincided with the onset of cracking strain
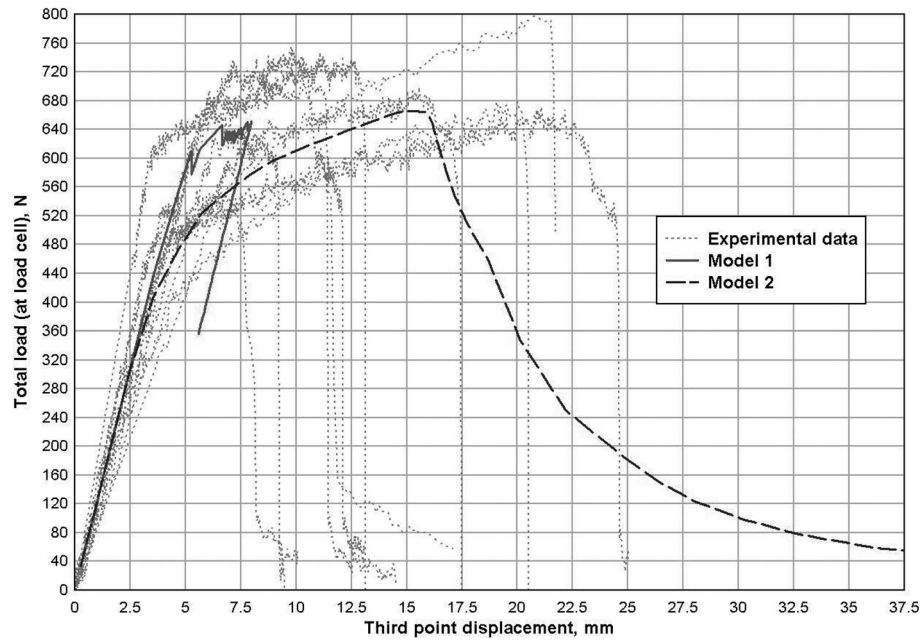
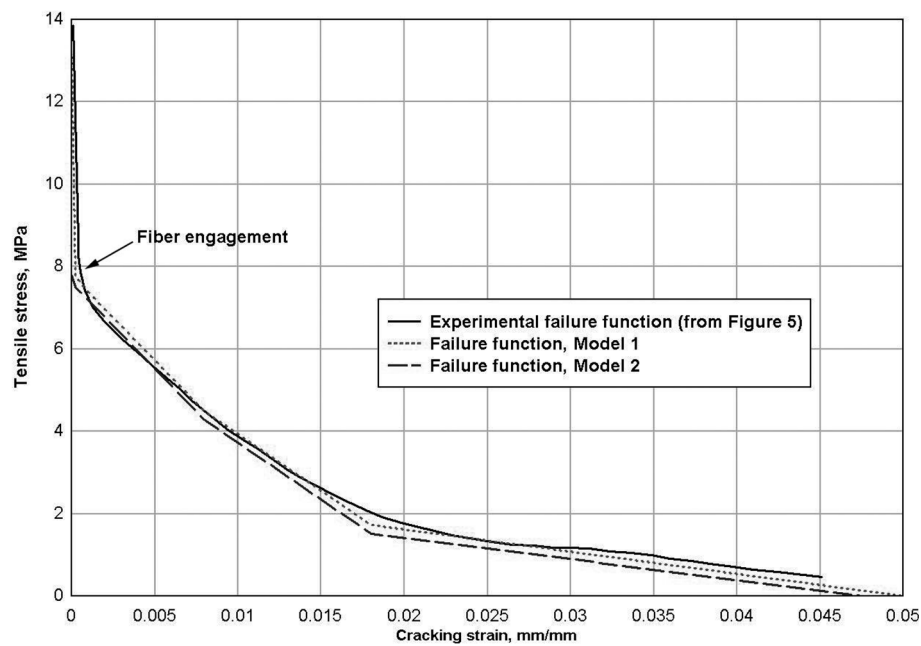Fig. 7 FE model results (flexure response analyses)



Fig. 8 Flexural FE model tensile failure functions

along the model's tension face. After formation of the sharp load-displacement transition, cracking strain began to grow in terms of magnitude and dispersion through the specimen, which resulted in a close match initially to the deflection-hardening response measured in the flexural experiments.

However, at a displacement of approximately 7.6 mm, the solution transitioned into elastic recovery and diverged from the experimental results as both load and displacement decreased along the slope of initial system stiffness.

Because of the onset of elastic recovery in Model 1, the second model without viscoplastic regularization was used. In order for the calculations to progress into the deflection-hardening response phase, it was necessary to truncate the initial matrix cracking portion of the prescribed tensile failure function for Model 2. Results for Model 2 are shown in Fig. 7, where two notable observations are made. First, a much softer transition between initial elastic and post first-crack response was calculated due to truncation of the concrete matrix cracking portion of the failure function. However, after transition to the softened response, post first-crack stiffness closely followed the experimental data. Furthermore, the model reasonably calculated the panel's ultimate failure at a load and displacement of 663 N and 16 mm, respectively, which can be compared to the mean experimental values from Table 1 of 676 N and 13.7 mm.

Notably, both models provided a deterministic calculation of the panels' response and failure, arriving at a single solution for the load-displacement response based on the given problem parameters. However, as observed in the experimental data, due to the random (and non-uniform) distribution of fibers within the material, the failure response was for more stochastic in nature. This indicates the need for a more stochastic numerical approach to calculation of the fiber-reinforced concrete's failure response, providing a means to consider the effects of fiber randomization within the material.

## 6. Conclusions

The purpose of this study was to investigate the flexural and tensile properties of a newly developed ultra-high-strength, glass fiber-reinforced concrete material. To perform the investigation, a coupled approach was followed which included (a) experimentation to determine the material's flexural and direct tension properties, (b) implementation of a micromechanically-based analytical model to consider the effect of mesoscale interactions on macroscale response, and (c) analysis of the flexural response using the finite element method and an experimentally determined tensile failure function.

From the flexural experiments, initial flexural modulus and first-crack strength were estimated to be 39 GPa and 13 MPa, respectively. Flexural response prior to first-crack was essentially linear, which was followed by a linear deflection hardening phase with significantly reduced stiffness (post-crack modulus of approximately 5.4 GPa). Moderate load increase during the deflection hardening response was observed (from the first-crack formation to ultimate failure), with the mean ultimate load 26 percent greater than the first-crack load. Significant variability was observed in the ultimate displacement at failure, with values ranging from approximately 6.5 mm to 24 mm. This was attributed to the random distribution of fibers throughout the material, highlighting the stochastic nature of the materials' failure response.

The direct tension experiments provided pre- and post-crack material characteristics for comparison to the flexural response data. Analysis of the direct tension data indicated an initial tensile modulus of 43 GPa, which was 10 percent greater than the flexural modulus. Due to the specimens' notched design, FE analysis was required to determine cracking strength of the material due to stress concentration effects. Therefore, ABAQUS was used to determine stress conditions in the test

specimen at peak tensile load, which indicated a material tensile strength of approximately 14.5 MPa. Compared to the flexural strength, the first-crack tensile strength was 12 percent greater. Lastly, the direct tension test data was used to characterize the material's strain softening response. Expressed in the form of tensile bridging stress versus crack opening width, data analysis indicated that failure initiated in the matrix at approximately 14.5 MPa and then sharply fell to a fiber bridging strength of approximately 7.8 MPa. Following fiber engagement, the material exhibited very limited ductility, achieving a maximum crack opening width of approximately 0.6 mm. Note that in consideration of the limited number of direct tension tests performed in this study, further testing is suggested to validate results.

To study the influence of fiber/matrix interaction on the UHS-GFRC's macroscale strain softening response, a series of micromechanical models were implemented. Utilizing a progressive approach, models were first presented to describe the fundamental interaction between a single fiber and the matrix, followed by probability-based models to predict the tensile failure response of cementitous composites reinforced with randomly distributed fibers. Ultimately, the models did not generate an accurate prediction of tensile failure in the UHS-GFRC material. The most notable difference was in the maximum crack opening width, in which the model predicted a maximum crack opening width of 12.7 mm (one-half of the fiber length), while a maximum crack width less than 1 mm was observed. The expected cause of this difference was telescoping of the glass fibers, where the inner glass strands pulled out of the fiber core, leaving only the perimeter strands to be bonded with the matrix. The effect of telescoping would be more rapid failure of the fibers (as compared to equivalent solid fibers) since only the perimeter strands provided tensile resistance. Because the micromechanical models were formulated for solid fiber materials (such as steel), this effect was not captured.

Although the micromechanical models did not accurately predict tensile failure response in the material, several qualitative observations were made. First, as just discussed, ductility in the material was very limited in comparison to that which would be expected for other fiber types. This was a result of the failure mode in the glass fibers, and therefore other fiber types could be considered to improve ductility. Also, the models indicated that a jump could be expected from the matrix cracking strength to the fiber bridging strength–the magnitude of which would be dependent on the fiber, matrix and interaction properties. Utilizing an interface bond strength of 12 MPa, the models estimated a maximum fiber bridging strength of 7.6 MPa. As a result, after matrix cracking a sharp strength loss from the first-crack strength (14.5 MPa) to the fiber bridging strength was predicted, which was in agreement with the experimental results.

Lastly, the finite element method was utilized to model flexural response of the panels based on the tensile failure function measured in the direct tension experiments. A concrete damage plasticity constitutive law was used, and the measured tensile failure function was used to describe the strain softening response. Due to model stability, two tensile failure definitions were implemented. The first definition directly used the experimental failure function, but also required the use of viscoplastic regularization to maintain stability during the softening response. The second definition truncated the strength drop from matrix cracking to fiber bridging strength, and did not use viscoplastic regularization. Results from both constitutive model definitions reasonably matched certain aspects of the experimental flexural response, although neither exactly calculated the observed response. From this, the need for further development of numerical methods to calculate the strain softening response of fiber reinforced concrete is observed. It is also noted that the FE model provided a deterministic solution, although the experimental data indicated that the fiber-

reinforced concrete's failure response was highly stochastic. Therefore, stochastic numerical techniques which consider the effects of fiber randomization are needed in order to accurately predict the range of failure responses that might occur.

## Acknowledgements

## References

ABAQUS/CAE, Version 6.5-4. (2005), SIMULIA, Providence, RI.

ABAQUS, Inc. (2004a), Version 6.5 Analysis User's Manual, Section 11.5.3, ABAQUS Online Documentation, Version 6.5-1.

ABAQUS, Inc. (2004b), Version 6.5 Theory Manual, Section 4.5.2, ABAQUS Online Documentation, Version 6.5-1.

ACI Committee 549 (2004), "Report on thin reinforced cementitous products", ACI 549.29-04, American Concrete Institute, Farmington Hills, MI.

ACI Committee 544. (1996), "Report on fiber reinforced concrete", ACI 544.1R-96, American Concrete Institute, Farmington Hills, MI.

Akers, S.A., Green, M.L. and Reed, P.A. (1998), "Laboratory characterization of very high-strength fiber-reinforced concrete", *Technical Report SL-98-10*, U.S. Army Corps of Engineers, Waterways Experiment Station, Vicksburg, MS.

ASTM C 109-07, "Standard test method for compressive strength of hydraulic cement mortars (using 2-in. [or 50-mm] cube specimens)", ASTM International, West Conshohocken, PA, 19428.

ASTM C 947-03, "Test method for flexural properties of thin-section glass-fiber reinforced concrete (using simple beam with third-point loading)", ASTM International, West Conshohocken, PA, 19428.

Balaguru, P., Narahari, R. and Patel, M. (1992), "Flexural toughness of steel fiber reinforced concrete", *ACI Mater. J.,* **89**(6), 541-546.

Banthia, N. and Gupta, R. (2004), "Hybrid fiber reinforced concrete (HyFRC): fiber synergy in high strength matrices", *Mater. Struct.*, **37**, 707-716.

Beghini, A., Bazant, Z.P., Zhou, Y., Gouirand, O. and Caner, F. (2007), "Microplane model M5F for multiaxial behavior of and fracture of fiber-reinforced concrete", *J. Eng. Mech.*, **133**(1), 66-75.

Bindiganavile, V., Banthia, N. and Aarup, B. (2002), "Impact response of ultra-high-strength fiber-reinforced cement composite", *ACI Mater. J.,* **99**(6), 543-548.

Chanvillard, G. and Rigaud, S. (2003), "Complete characterisation of tensile properties of Ductal® UHPFRC according to the French recommendations", *Fourth International Workshop on High Performance Fiber Reinforced Cement Composites (HPFRCC4)*, Ann Arbor, MI, June 15-18, 2003. RILEM Publications, A.E. Naaman and H.W. Reinhardt, eds., Bagneux, France, 21-34.

Giaccio, G. and Zerbino, R. (2002), "Fiber reinforced high strength concrete: evaluation of failure mechanism", *High Performance Concrete, Performance and Quality of Concrete Structures (Proceedings, Third International Conference, Recife, PE, Brazil)*, V.M. Malhotra, P. Helene, E.P. Figueirdo, and A. Carneiro, ed., ACI Special Publication, **207**, 69-89.

Kabele, P. (2002), "Equivalent continuum model of multiple cracking", *Eng. Mech. (Association for Engineering Mechanics, Czech Republic)*, **9**, 75-90.

Kabele, P. (2003), "New developments in analytical modeling of mechanical behavior of ECC", *J. Adv. Concr Technol.*, **1**(3), 353-264.

Kabele, P. (2007), "Multiscale framework for modeling of fracture in high performance fiber reinforced cementitous composites", *Eng. Fract. Mech.*, **74**, 194-209.

Kanda, T. and Li, V.C. (1999), "Effect of fiber strength and fiber-matrix interface on crack bridging in cement composites", *J. Eng. Mech.*, **125**(3), 290-299.

Lee, J. and Fenves, G.L. (1998), "Plast-damage model for cyclic loading of concrete structures", *J. Eng. Mech.*, **24**(8), 892-900.

Li, V.C. (1992), "Postcrack scaling relations for fiber reinforced concrete cementitous composites", *J. Mater. Civil Eng.*, **4**(1), 41-57.

Li, V.C. and Stang, H. (1997), "Interface property characterization and strengthening mechanisms in fiber reinforced cement based composites", *Adv. Cem. Based Mater.*, **6**, 1-20.

Li, V.C., Stang, H. and Krenchel, H. (1993), "Micromechanics of crack bridging in fibre-reinforced concrete", *Mater. Struct.*, **26**, 486-494.

Li, V.C. and Wang, S. (2006), "Microstructure variability and macroscopic composite properties of high performance fiber reinforced cementitious composites", *Probabilist. Eng. Mech.*, **21**, 201-206.

Li, V.C., Wang, Y. and Backer, S. (1991), "A micromechanical model of tension-softening and bridging toughening of short random fiber reinforced brittle matrix composites", *J. Mech. Phys. Solids*, **39**(5), 607-625.

Li, V.C., Wu, H., Maalej, M., Mishra, D.K. and Hashida, T. (1996), "Tensile behavior of cement-based composites with random discontinuous steel fibers", *J. Am. Ceram. Soc.*, **79**(1), 74-78.

Lubliner, J., Oliver, J., Oller, S. and Onate, E. (1989), "A plastic-damage model for concrete", *Int. J. Solids Struct.*, **25**(3), 229-326.

Maalej, M., Li, V.C. and Hashida, P. (1995), "Effect of fiber rupture on tensile properties of short fiber composites," *J. Eng. Mech.*, **121**(8), 903-913.

Nelson, P.K., Li, V.C. and Kamada, T. (2002), "Fracture toughness of microfiber reinforced cement composites", *J. Mater. Civil Eng.*, **14**(5), 384-391.

Ngo, T., Mendis, P., Lam, N. and Cavill, B. (2005), "Performance of ultra-high strength concrete panels subjected to blast loading", *Science, engineering and technology summit,* Canberra, Australia, 2005. P. Mendis, J. Lai, and E. Dawson, ed., Research Network for a Secure Australia, 193-208.

O'Neil, E.F., III, Cummins, T.K., Durst, B.P., Kinnebrew, P.G., Boone, R.N. and Toores, R.X. (2004), "Development of very-high-strength and high-performance concrete materials for improvement of barriers against blast and projectile penetration", *U.S. Army Science Conference,* Orlando, FL, December 2004.

O'Neil, E.F., Neeley, B.D. and Cargile, J.D. (1999), "Tensile properties of very-high-strength concrete for penetration-resistant structures", *Shock Vib.,* **6**, 237-245.

Roth, M.J. (2008), *Flexural and tensile properties of thin, very high-strength, fiber-reinforced concrete panels*, Technical Report ERDC/GSL TR-08-24, U.S. Army Engineer Research and Development Center, Vicksburg, MS 39180.

Shah, S.P. (1997), "Material aspects of high performance concrete", *High Strength Concrete – First International Conference*, Kona, HI, July 13-18, 1997, A. Atorod, D. Darwin, and C. French, eds., ASCE, Reston, VA, 504-516.

Wang, Y., Li, V.C. and Backer, S. (1990), "Experimental determination of tensile behavior of fiber reinforced concrete", *ACI Mater. J.*, **87**(5), 461-468.

Williams, E. Graham, S., Reed, P. and Rushing, T. (2009), "Laboratory characterization of Cor-Tuf with and without steel fibers", *technical report in preparation*, U.S. Army Corps of Engineers, Waterways Experiment Station, Vicksburg, MS.

Zheng, W., Kwan, A.K.H. and Lee, P.K.K. (2001), "Direct tension test of concrete", *ACI Mater. J.*, **98**(1), 63-71.